optica

Infrared nanospectroscopic imaging in the rotating frame: supplementary material

SAMUEL C. JOHNSON[1], ERIC A. MULLER[1], OMAR KHATIB[1], ELISA A. BONNIN[2], ALEXANDER C. GAGNON[2], AND MARKUS B. RASCHKE[1,*]

[1]Department of Physics, Department of Chemistry, and JILA, University of Colorado, Boulder, CO 80309, USA
[2]School of Oceanography, University of Washington, Seattle, WA 98195, USA
[*]Corresponding author: markus.raschke@colorado.edu

Published 3 April 2019

This document provides supplementary information to "Infrared nanospectroscopic imaging in the rotating frame," https://doi.org/10.1364/OPTICA.6.000424. We discuss below details of R-sSNOM and its comparison to multiple imaging and spectroscopy modalities of *s*-SNOM. Specifically, we elaborate on data processing, artifact free imaging, comparison to other scanning probe techniques, theoretical considerations and sample preparation for the near-field imaging of biomineralized samples.

1. INTRODUCTION

Here, we offer further details, derivation and insight into the topics covered in *Infrared Nano-Spectroscopic Imaging in the Rotating Frame*. We further elaborate on the passive drift correction, replacing dropped pixels, processing interferograms, modifications to the reference arm in a conventional *s*-SNOM measurement. We show additional data and nano-imaging of the Amide response. Then we discuss other background free spatio-spectral methods and compare them to R-sSNOM and conventional Fourier Transform detection. Next, we elaborate on spectral contamination introduced by measuring at the Nyquist limit and artifacts resulting from the rotation process. Theoretical considerations for Fourier transform spectroscopy in multiple bases are considered and discussed. Finally, specifics about sample preparation and the resulting effects are given in detail.

2. DATA PROCESSING

A. Drift Correction

Over the course of data acquisition, depending on the thermal stability of the AFM stage, the sample drifts relative to the tip. This is typically in the range of a few hundred nanometers per hour. To compensate for this, we use a homemade post processing passive drift correction. Instead of measuring and tracking a fiducial marker, we use the height data channel already collected when taking AFM scans in the multi-step 2 phase homodyne data collection. We calculate the cross correlation in Fourier space using the first mirror step position as the reference. We then search for the pixel with the highest cross correlation and generate a running drift vector. We then use this dictionary to stack the X and Y data channels, corresponding to the drift of the accompanying height channel such that the drift is removed. We then crop all images in the stack so that only the pixels shared in all images are kept.

B. Dropped Pixel Correction

The *s*-SNOM pixel quality in each mirror position depends on the combination of the stability of the laser output, chopper frequency, AFM tip frequency and the demodulation of these frequencies. When there is an instability in one or more of these components, the image being taken loses data for at least a pixel. This manifests itself in an unusually high demodulation value, typically from the lock-in detecting a low frequency noise component, that is easily seen by eye. To correct for this, a series of operations are performed. First, from our duplicity of data for each X and Y channel, if a pixel is dropped on either a trace or retrace scan, but not the other, the pixel can be filled in using the other direction's pixel value. Second, each image is analyzed to identify pixels above a given threshold, when one is found, the pixel is replaced by the average of the surrounding 8 pixels. Finally, the remaining dropped pixels are isolated pixels below the conservative threshold, but they are clearly still not accurate. Each image is scanned for isolated pixels that strongly deviate from the mean of the surrounding pixels, and again, these pixels are replaced with the mean of the surrounding pixels. A standard 4,000 pixel image has approximately 10 dropped pixels.

C. FTIR Processing

Interferograms from either method of data acquisition are processed in the same way. The data vector is first zero-padded

asymmetrically such that the length of the vector is a power of 2 and approximately 4 times as long and are added such that the center-burst is in the middle of the vector. This has the effect of increasing the speed at which the FFT runs and interpolating the data in frequency space. The vector is then apodized with a Blackman-Harris function to further increase the signal to noise of the data in frequency space. The interferogram is inverted and Fourier transformed, using Matlab's native FFT algorithm. We then reference the output spectrum to a chosen spectrum from a non-resonant sample such as template stripped Au as described in detail above. Here, for robust and clear Amide I response, we reference to an average phase response from a known calcite region. This has the effect of compensating for the tail end of the much stronger calcite peak, yielding a purely Amide response. Note that different strengths from topographic defects of the calcite response yields a non-uniform phase response at the calcite tail. Using a typical calcite response limits these artifacts to a few pixels which are easily confirmed to be amide free by examining the individual spectra.

3. ARTIFACT FREE IMAGING

A. Reference Arm Modifications

To reduce far-field illumination artifacts and to increase acquisition speed, two modifications are made to the reference arm of a typical *s*-SNOM setup. The first modification is inserting a chopper wheel into the reference arm, giving a characteristic frequency to E_{REF}; it should be noted that the selection of blade size relative to beam size greatly impacts the distribution of the frequency components added to the electric field. To isolate the heterodyne interference term at the detector, we demodulate at the chopper frequency plus the second harmonic tip frequency, which isolates the near-field signal directly amplified by the reference arm from far field or background electric field contamination.[1] The second modification is to use a piezo actuated mirror mount for the reference arm mirror. By adding a piezo, we have fast, reproducible and stable control of our mirror position at mesoscale distances. This is used in conjunction with the typical long range stage used for stationary frame spectroscopic purposes.

B. Additional Dataset

Figure S1 shows rotating frame applied to another area of the prismatic region. Here, the X and Y axes are the relative positions across the sample's surface and the Z axis shows the topography of the sample at each of these points. The colormap shows the relative strength of the phase response at 1680 cm^{-1} response typical of Amide, indicating the presence of proteins, in good agreement with the organic ridge formed by the etching process.

4. COMPARISON TO CONVENTIONAL *S*-SNOM IMAGING

A. Resolution Line-Cuts

Figure S2c shows the marked spatial resolution improvement of the rotating frame (Fig. S2a) compared to the stationary frame (Fig. S2b) by taking corresponding line-cuts from the Amide slice images and comparing their slopes at the edge of a feature of interest. In terms of time, and correspondingly useable data points, along with accurate sample positions, this represents a non-trivial and marked improvement upon previous hyperspectral imaging modalities.

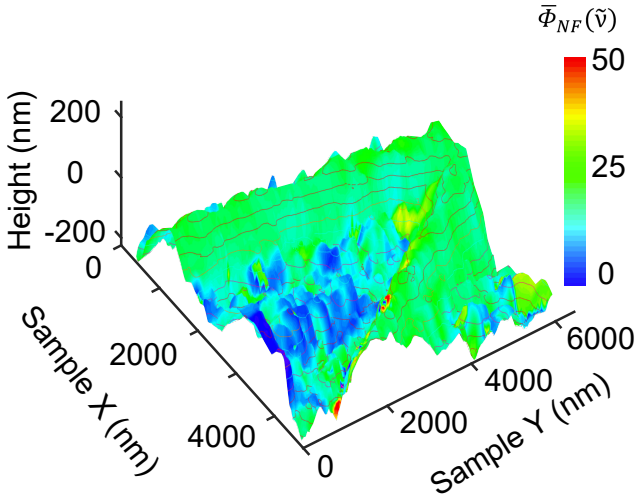

Fig. S1. Spatial Resolution | Additional rotating frame data set acquired in the prismatic region of an Oyster shell showing a high protein concentration in a V-shaped region as determined by the Amide I response.

B. Lineshape Contamination

The slight deviation of the phase response (1680 cm^{-1}) from a typical *s*-SNOM experiment is a result of the inverse mirror symmetry associated with the phase from the Fourier transform. This symmetry necessitates a strong turning point near 1750 cm^{-1} and leads to a small contamination in the absolute spectral position, and shape, of the resonance. This effect can be minimized by choosing a larger bandwidth for the rotation, or shifting the incident light source frequency such that the rotated resonance frequency is smaller than shown. Here however, the resonance is so broad that the laser cannot be further blue shifted. Additionally, for chemical mapping of extremely broad resonances, like the Amide response, the only necessary consideration is resonance identification which is not affected to a measurable degree by the the shifting of a peak center by $\sim$10 cm^{-1}. It should also be noted that this shifting is on the order of typical peak shifts across these biological samples, further making the peak assignment reasonable.

5. THEORETICAL CONSIDERATIONS

A. Rotating Frame Theory

We first consider the standard *s*-SNOM detected signal and contrast this with the rotating frame approach through subsampling data collected in the conventional manner. Second, we compare pseudo-heterodyne and chopper demodulated 2 phase homodyne as detection schemes for implementing the rotating frame. Finally, we apply the rotating frame technique to investigate the nanoscopic prismatic region in an oyster shell. Equation S1 demonstrates the near-field heterodyne amplified intensity of the scattered light in the x demodulated channel of the lock-in in frequency space.

$$I_{\mathrm{x}}(k) = \sum_{n=0}^{N_{\mathrm{STAT}}-1} e^{\frac{-2\pi i}{N_{\mathrm{STAT}}} k \tilde{x}_{\mathrm{n}}(t)} I_{2\mathrm{H}}(\tilde{x}_{\mathrm{n}}(t)) \qquad \text{(S1)}$$

Here, N_{STAT} is the number of data points collected along the interferogram, k is the output frequency of the transform, $\tilde{x}$ is the position of the interferometer arm (where n is the sampling

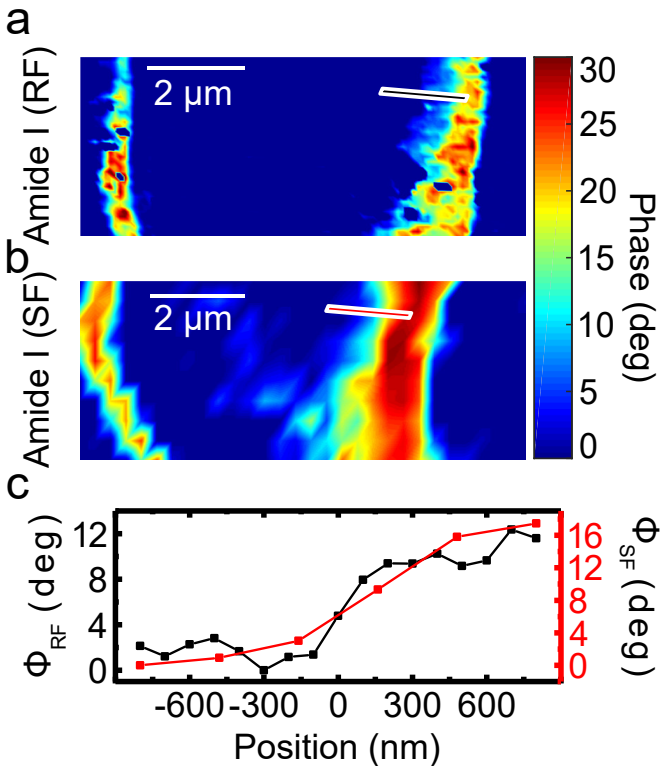

Fig. S2. Spatial Resolution | **a**, Rotating frame phase response at 1680 cm^{-1}. **b**, Stationary frame phase response at 1680 cm^{-1}. **c**, Feature edge comparison between rotating and stationary frame Amide I phase response at regions indicated in panels a and b.

number — position index). We then normalize our complex valued response from our sample of interest by dividing it by the complex valued reference spectrum. The minimum value N_{STAT} can take is given by the Nyquist sampling theorem and for our laser, centered at 1680 cm^{-1}, (and a resolution of 20 cm^{-1}) is 181. In the rotating frame we now measure the relative optical frequency, as shown in equation S2.

$$I_x(k-k_0) = \sum_{n=0}^{N_{ROT}-1} e^{\frac{-2\pi i}{N_{ROT}}(k-k_0)(\tilde{x}_n(t)+\tilde{\phi})} I_{2H+\Omega}(\tilde{x}_n(t)) \quad \text{(S2)}$$

Where we have included the subtracted frequency k_0, a mirror position offset $\tilde{\phi}$ (controlled by the reference mirror piezo) and Ω the chopper frequency. Again, the minimum value N_{ROT} can take is given by the Nyquist sampling theorem. This time though, $\tilde{x}_n - \tilde{x}_{n-1}$ determines the maximum cut-off frequency, which we choose to be approximately $3 * \Gamma_{vib}$. Therefore, the minimum value N_{ROT} can take (for a resolution of 20 cm^{-1}) is 21 — a reduction by almost an order of magnitude. While the minimum sampling number is lowered by approximately an order of magnitude, the typical hyper-spectral imaging modality cannot leverage this reduction in data points to faster data acquisition.[2, 3] To utilize the reduction granted by transforming to the rotating frame, we borrow an imaging technique created for CW sources.[4] In the rotating frame, we shift the frequency response, but still need a mechanism for background free imaging and DC offset subtraction. Two phase chopper demodulated homodyne has previously been shown to effectively extract both the amplitude and phase response of a material under illumination of a single wavelength source.[1] By employing this technique and simultaneously scanning the reference arm, we are able to extract the amplitude and phase response for every frequency contained in our source. Pseudo-heterodyne with a broadband light source has a normalization condition between the real and imaginary channels of the near-field response that is non-trivial to tease out and further complicated by being extremely sensitive to experimental parameters. Pseudo-heterodyne, while theoretically possible, is not a practical method for background suppression in broadband *s*-SNOM hyper-spectral imaging.[5] The detected signal when using a broadband source with pseudo-heterodyne is given by equation S3.

$$\begin{aligned} I(\omega) = \int_{-\infty}^{\infty} dt e^{-i\omega t} e^{\frac{-2\sigma^2\epsilon^2}{c^2}} \int_{\omega_1}^{\omega_2} d\omega_0 e^{-i\omega_0 t} \\ e^{\frac{-i2\omega_0\epsilon}{c}} e^{\frac{-2\sigma^2}{c^2}(\epsilon\xi\sin(mt+\phi_m)+\xi^2\sin^2(mt+\phi_m))} \alpha_{eff}(\omega_0,t)* \\ [J_0(2\omega_0\xi) + 2\sum_{n=1}^{\infty}(J_{2n}(2\omega_0\xi)\cos(2n(mt+\phi_m)) + \\ iJ_{2n-1}(2\omega_0\xi)\sin((2n-1)(mt+\phi_m)))] \end{aligned} \quad \text{(S3)}$$

Here, we see a complex interplay between the laser specifications, including ω_0=laser carrier frequency and σ=laser bandwidth, the reference mirror motion, including ξ=mirror oscillation amplitude, ϕ_m=mirror phase offset and m=mirror oscillation frequency and the near-field response (as modeled by α_{eff}=effective complex polarizability). Broadband pseudo-heterodyne contains a complicated mixing of real and imaginary sidebands dependent on how the parameters listed above interact.

Immediately obvious is the increased complexity of pseudo-heterodyne interferograms when compared to stationary frame (Fig. S3a) and rotating frame (Fig. S3b) interferograms. Depending on the mirror position, the center frequency, and the bandwidth of the light source, the real and imaginary near-field response start mixing. Figure S3c shows this behavior. The complicated (non-slowly varying) waveform in the rotating frame (Fig. S3d) doesn't solve our problem of reducing the acquisition distance (mirror step size). We therefore select multi-step chopper-demodulated two-phase homodyne for our background suppression and DC offset correction.

B. Pseudo-Heterodyne

For pseudo-heterodyne background suppression the sidebands are generated through the Jacobi-Anger expansion that results from argument of the electric field that depends on the sinusoidal motion of the reference arm mirror. This results in, relative to center frequency, positive and negative sidebands with weight defined by the expansion coefficients, which for the case of single wavelength sources, can be paired such that each pair of neighboring sidebands has the same maximal value. Experimentally, this means as the reference mirror is scanned, the relative populations of the first two sidebands oscillate to a shared maximum out of phase. This is complicated however when the source has a non-negligible bandwidth. We see that in addition to the difficulty of scaling the waveforms generated by pseudo-heterodyne (and it being phase dependent — impossible to do in general for a broadband source), there is a complicated secondary envelope

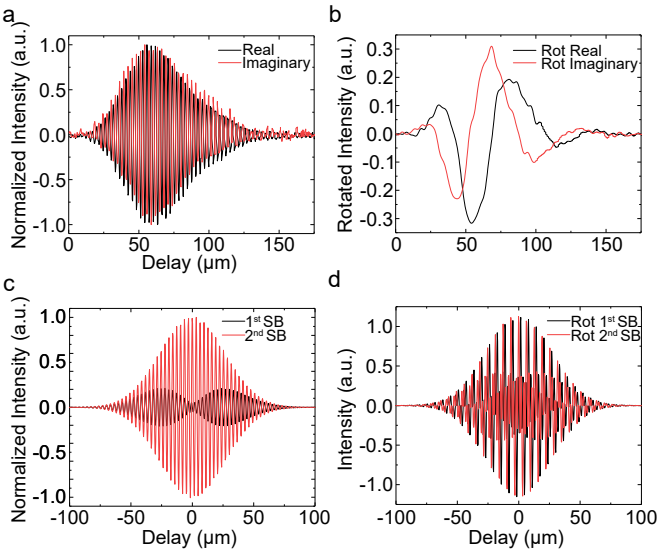

Fig. S3. Method of Accessing Rotation Basis | **a**, Experimental data of two typical interferograms as two basis vectors to span rotation space collected using the fine delay mirror control. **b**, Rotated interferograms of experimental data in panel a. **c**, Resonance-less model data generated by computing pseudo-heterodyne data collected by demodulating at the second harmonic of the cantilever frequency and the 1st and 2nd sidebands (SB). **d**, Rotating frame applied to interferogram basis vectors acquired through pseudo-heterodyne.

function for the two sidebands. Again, while it is theoretically possible to deconvolve this mixing, the experimental nature of crucially determining these parameters with stability on the few to 10s of hours timescale is simply not practical. Additionally, assuming the deconvolution could be done, the Jacobi-Anger expansion splits the near-field signal into an infinite series of sidebands, diluting the signal to channels that are discarded and decreasing the relative signal to noise compared to a method that creates sidebands of finite (or faster converging) order. From these considerations the choice for background free imaging between pseudo-heterodyne and chopper demodulation should clearly be the latter.

6. METHODS - SAMPLE PREPARATION

Shells of the Pacific Oyster (Crassostrea gigas) were cleaned of tissue by hand, rinsed with water, and stored in a freezer prior to sampling. Both valves of C. gigas contain prismatic layers, but this layer is thickest and easiest to locate in the right valve [6]. The prismatic layer is located between an outer organic coating, called the periostracum, and inner chalky and foliated layers. In C. gigas, the prismatic layer, chalky layer, and foliated layer are all primarily made of calcite, the most stable polymorph of $CaCO_3$. Portions of a right valve were sampled by hand using a rotary tool (Dremal) fitted with a diamond-impregnated disc. These sections include the full thickness of the shell. Because it is difficult to section in a perfectly longitudinal plane, the resulting surface is oblique with respect to the columns. The sections were mounted on a round glass slides ($\varnothing \sim 2.5$ cm) using Araldite 502 resin (Pelco), and polished with progressively smaller diamond grit sizes, ranging from 60 μm to 0.15 μm (Beta Diamond and 3M), in a slurry with water. Ultrasonication in 18 MΩ pure water when switching between polishing grit sizes removed residual grit. After polishing, the organic sheaths of the prismatic layer were topographically exposed using a quick ($\sim$3 second) and mild (0.1 M HCl) etch.

REFERENCES

1. S. Berweger, D. M. Nguyen, E. A. Muller, H. A. Bechtel, T. T. Perkins, and M. B. Raschke, "Nano-Chemical Infrared Imaging of Membrane Proteins in Lipid Bilayers," J. Am. Chem. Soc. **135**, 18292–18295 (2013).
2. B. Pollard, E. A. Muller, K. Hinrichs, and M. B. Raschke, "Vibrational nano-spectroscopic imaging correlating structure with intermolecular coupling and dynamics," Nat. Commun. **5**, 3587 (2014).
3. I. Amenabar, S. Poly, M. Goikoetxea, W. Nuansing, P. Lasch, and R. Hillenbrand, "Hyperspectral infrared nanoimaging of organic samples based on Fourier transform infrared nanospectroscopy," Nat. Commun. **8**, 14402 (2017).
4. B. Pollard and M. B. Raschke, "Correlative infrared nanospectroscopic and nanomechanical imaging of block copolymer microdomains," Beilstein J. Nanotechnol **7**, 605–612 (2016).
5. A. J. Sternbach, J. Hinton, T. Slusar, A. S. Mcleod, M. K. Liu, A. Frenzel, M. Wagner, R. Iraheta, F. Keilmann, A. Leitenstorfer, M. Fogler, H.-T. Kim, R. D. Averitt, and D. N. Basov, "Artifact free time resolved near-field spectroscopy," Opt. Express **25**, 28589–28611 (2017).
6. J. Macdonald, A. Freer, and M. Cusack, "Alignment of Crystallographic c-Axis throughout the Four Distinct Microstructural Layers of the Oyster Crassostrea gigas," Cryst. Growth & Des. **10**, 1243–1246 (2010).